Dynamic response of elliptical cylinders undergoing transverse flow-induced vibration

Jisheng Zhao [*], Kerry Hourigan, Mark C. Thompson

Fluids Laboratory for Aeronautical and Industrial Research (FLAIR), Department of Mechanical and Aerospace Engineering, Monash University, Victoria 3800, Australia

ARTICLE INFO

ABSTRACT

While the flow-induced vibration (FIV) of a circular cylinder has been characterised in considerable detail, the FIV of elliptical cylinders has not received similar attention. This study investigates the dynamic response of elastically-mounted elliptical cylinders with various cross-sectional aspect ratios (or elliptical ratios) in a free stream. The elliptical ratio is defined by $\epsilon = b/a$, where a and b are the streamwise and cross-flow dimensions, respectively, of the cross section of a cylinder placed at zero incidence angle. The elliptical ratios tested were in the restricted range of $0.67 \leqslant \epsilon \leqslant 1.50$, which was designed to achieve some but not too large a geometric deviation from a circular cylinder. The fluid–structure system was modelled using a low-friction air-bearing rig in conjunction with a free-surface recirculating water channel facility. This experimental set-up yielded very low mass and damping ratios. The FIV response was characterised as a function of reduced flow velocity. The results showed that the ellipses exhibited different response regimes as ϵ varied. Surprisingly, for the lowest elliptical ratio $\epsilon = 0.67$, there existed two separated lock-in regimes. However, for $\epsilon \geqslant 0.80$, lock-in occurred over only a single reduced velocity range that was characterised by different response regimes. As ϵ was increased above unity, lock-in tended to occur at considerably lower reduced velocities than for the circular cylinder case. Moreover, the peak vibration amplitude increased with the elliptical ratio. This means that the body vibration is enhanced, rather than attenuated, as the afterbody is reduced for an ellipse.

© 2019 Elsevier Ltd. All rights reserved.

1. Introduction

Flow-induced vibration (FIV) of structures is of great interest in a large variety of engineering applications, due to its being both a potential energy harvesting source (see Wang et al., 2017; Soti et al., 2018) and as an undesirable phenomenon that can result in structural fatigue and even lead to catastrophic failures (e.g. the collapse of the original Tacoma Narrows Bridge in 1940). In the last half century, extensive investigations have been motivated to characterise, predict and control flow-induced vibration, as collected in the review articles of Bearman (1984), Sarpkaya (2004), Williamson and Govardhan (2004), Gabbai and Benaroya (2005) and the books of Blevins (1990), Naudascher and Rockwell (2005) and Païdoussis et al. (2010).

The circular cylinder has been adopted as the canonical model in numerous studies of the FIV subject (e.g. Brooks, 1960; Feng, 1968; Khalak and Williamson, 1996; Govardhan and Williamson, 2000; Carberry et al., 2005; Morse and Williamson, 2009; Zhao et al., 2014a, to only name a few), owing mainly to its geometric simplicity and symmetry and also practicality

---

in engineering applications (such as offshore pipelines and oil risers, transmission cables, wind turbine towers, and cooling tubes in nuclear power plants). From the fundamental point of view, the axial symmetry allows one form typical of FIV, *vortex-induced vibration (VIV)*, to be studied independently from other forms of FIV, e.g. galloping. VIV is linked to vortices shed periodically from both sides of an elastic or elastically-mounted body, which in turn exert oscillating pressures on the body to cause structural vibration. If the vortex shedding frequency is near the natural frequency of the structural system, a nonlinear resonance phenomenon known as synchronisation (or "lock-in") can be encountered with large-amplitude body oscillations. It has been shown that the synchronisation range depends on the mass and damping ratios (see Feng, 1968; Khalak and Williamson, 1996; Govardhan and Williamson, 2006). Here the mass ratio (m^*) is defined as the ratio of the total oscillating mass (m) to the displaced fluid mass (m_d), namely $m^* = m/m_d$. On the other hand, however, a structure that lacks axial symmetry (e.g. ice-coated transmission cables in winds Den Hartog, 1932) may be susceptible to *galloping*, as opposed to, or in a combination with, VIV (see Bearman et al., 1987; Nemes et al., 2012; Zhao et al., 2014b, 2018c). Galloping is often referred to as an aeroelastic instability that is caused by changes in the relative incidence angle induced by the body motion resulting in aerodynamic forces in the same direction as the body motion (Naudascher and Rockwell, 2005). The studies of Nemes et al. (2012) and Zhao et al. (2014b) investigating the influence of angle on the transverse FIV of a square cylinder with low mass–damping ratios suggested that the afterbody (i.e. the structural part of a body downstream of the flow separation points) and the flow separation points were the key factors resulting in different vibration responses of VIV, galloping, and combined VIV and galloping. More recently, Zhao et al. (2018a) have shown in their study of D-section cylinders that an afterbody plays an important role affecting the FIV response, but it is not essential for VIV at low mass and damping ratios. Of interest to the present study is the transverse FIV response of elliptical cylinders with cross-sectional aspect ratios (or elliptical ratios) near unity that exhibit some but not too large a geometric deviation from the circular cylinder and thereby the afterbody is changed to some extent. This would also be of interest from the practical point of view as engineering applications often involve flow past elliptical or elliptical-like structures, such as wings and turbine blades. It should be noted that in the present study the elliptical ratio is defined by $\epsilon = b/a$, where a and b are the streamwise and cross-flow (transverse) dimensions, respectively, of an ellipse placed at zero incidence angle; for a circular cylinder, ϵ is equal to 1, with a and b being the cylinder diameter.

To date, while flow past stationary elliptical cylinders has received considerable attention, very little work has been conducted on the FIV of elliptical cylinders. Many previous studies, including (Lindsey, 1938; Ota et al., 1987; Nair and Sengupta, 1997; Johnson et al., 2004; Kim and Sengupta, 2005; Kim and Park, 2006), have shown that the pressure distributions, fluid forces and the vortex shedding frequency are greatly influenced by the aspect ratio, flow incidence angle and the Reynolds number. Note that the Reynolds number in this study is defined by $Re = Ub/\nu$, where U is the free-stream velocity and ν is the kinematic viscosity of the fluid. Moreover, the wake structure and instability have also been investigated via low-Reynolds-number ($\lesssim 400$) numerical simulations by Johnson et al. (2004), Sheard (2007), Thompson et al. (2014), Leontini et al. (2015) and Rao et al. (2017) showing that a rich variety of wake modes and transitions are encountered as the geometric shape, orientation and the Reynolds number are changed. In the case of transversely oscillating elliptical cylinders, Okajima et al. (1975) measured the aerodynamic forces and pressures exerted on an elliptical cylinder of $\epsilon = 0.2$ undergoing driven oscillations over a wide range of Reynolds numbers from 80 to 20 000. In their numerical simulations, D'Alessio and Kocabiyik (2001) showed that the wake patterns and fluid force coefficients of a driven elliptical cylinder of $\epsilon = 2$ were dependent on the inclined angle and the forcing oscillation frequency ratio. Franzini et al. (2009) found in experiments that the peak vibration amplitude of an elliptical cylinder undergoing VIV was considerably lower than that of a circular cylinder for $2000 \leqslant Re \leqslant 8000$. Yogeswaran et al. (2014) numerically investigated the VIV of elliptical cylinders with $0.7 \leqslant \epsilon \leqslant 1.43$ and $m^* = 10$ in laminar flows ($60 \leqslant Re \leqslant 140$), and found that the peak vibration amplitude increased with ϵ. More recently, Leontini et al. (2018) presented a parametric study, again at a low Reynolds number of $Re = 100$, to characterise the FIV response and wake modes of an ellipse of $\epsilon = 1.5$ with a low mass ratio of $m^* = 1$ as a function of the angle of attack ($0° \leqslant \alpha \leqslant 90°$) and flow reduced velocity ($2 \leqslant U^* = U/(f_n b) \leqslant 14$, with f_n the natural frequency).

In summary, the previous studies, mostly of low-Re numerical simulations, have shown that the FIV response of elliptical cylinder is strongly dependent on a number of factors, including the aspect ratio, reduced velocity, Reynolds number and mass ratio. However, a clear gap in the literature is the lack of detailed knowledge of the FIV response of ellipses at moderate Reynolds number. This study aims to provide a better understanding of the influence of the geometry of elliptical cylinders on the structural response, by varying the elliptical ratio. This study therefore aims to experimentally examine the dynamic response of low-m^* elliptical cylinders with various aspect ratios ($0.67 \leqslant \epsilon \leqslant 1.50$) as a function of reduced velocity at moderate Reynolds number.

The article proceeds by describing the experimental method in Section 2. The results and discussion on the dynamic responses are presented in Section 3. Finally, conclusions are drawn in Section 4.

2. Experimental method

2.1. Modelling of the fluid–structure system

A schematic of the one-degree-of-freedom (1-DOF) transverse FIV of an elliptical cylinder is shown in Fig. 1. The body dynamics is governed by the linear second-order oscillator equation

$$m\ddot{y}(t) + c\dot{y}(t) + ky(t) = F_y(t), \tag{1}$$

where m is the total oscillating mass of the system, c is the structural damping of the system, k is the spring constant, $y(t)$ is the body displacement, and $F_y(t)$ represents the transverse fluid force.
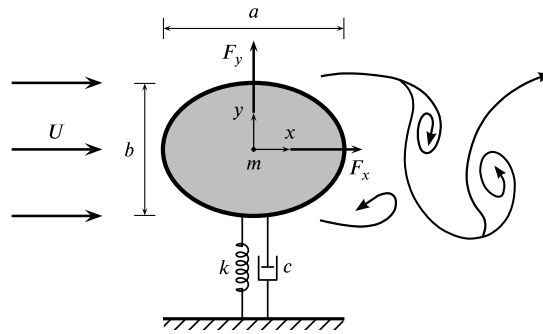
Fig. 1. A definition sketch of the problem studied: an elliptical cross-sectional cylinder constrained to oscillate across the free stream.

Table 1
The experimental parameters of the elliptical cylinders used in the present study.

ϵ	a [mm]	b [mm]	m [g]	m_d [g]	f_{na} [Hz]	f_{nw} [Hz]	ζ
0.67	30.00	20.00	1729.2	288.2	0.690	0.616	0.95×10^{-3}
0.80	25.00	20.00	1442.4	240.4	1.039	0.940	1.03×10^{-3}
1.00	25.00	25.00	1799.3	300.6	0.554	0.514	1.29×10^{-3}
1.25	20.00	25.00	1442.4	240.4	1.039	0.972	1.07×10^{-3}
1.50	16.67	25.00	1201.8	200.3	1.137	1.086	1.22×10^{-3}

2.2. Experimental details

The fluid–structure system was modelled based on a low-friction air-bearing system in conjunction with the free-surface recirculating water channel of the *Fluids Laboratory for Aeronautical and Industrial Research (FLAIR)*, Monash University. The test section of this water channel has dimensions of 600 mm in width, 800 mm in depth and 4000 mm in length (Zhao et al., 2014a,b).

In the present study, five elliptical cylinders with the elliptical ratio ($\epsilon = b/a$) ranging from 0.67 to 1.5 were tested. These rigid cylinder models were made from aluminium, using precision computer numerical control (CNC) and electrical discharge machining (EDM) to manufacture elliptical cross-sectional profiles with a tolerance of ± 0.010 mm. The cylinders were hard anodised against water corrosion. The immersed length of the cylinder was $L = 614$ mm, giving an aspect ratio (L/b) greater than 24.0. The total oscillating mass (m) and the displaced mass of the fluid ($m_d = \rho \pi abL/4$, with ρ the density of water) for all the cylinder cases are given in Table 1. The mass ratio, defined by $m^* = m/m_d$, was set equal to 6.0 for all the cases. This was limited by the minimum achievable value of the thinnest ellipse. The test cylinder model was vertically adapted to a low-friction air bearing rig, which was placed atop and transverse to the water channel. More details of the air-bearing system can be found in the related studies of Wong et al. (2017, 2018), Zhao et al. (2018a,b) and Sareen et al. (2018a,b,c). The opposite free ends of the cylinder models were set to have a small clearance (≈ 1 mm) above a conditioning platform to reduce end effects (see Khalak and Williamson, 1996; Zhao et al., 2014b, 2018a).

The natural frequencies of the system were measured by conducting free-decay tests individually in air and in quiescent water. Table 1 shows measurements of the natural frequencies in air (f_{na}) and in water (f_{nw}), together with the structural damping ratio and the cross-sectional dimensions of the ellipses tested. It should be noted that the damping ratio is determined with consideration of the added mass (m_A) by $\zeta = c/2\sqrt{k(m + m_A)}$, in which $m_A = ((f_{na}/f_{nw})^2 - 1)m$. Accordingly, the spring constant and damping factor could be determined by $k \simeq (2\pi f_{na})^2 m$ and $c = 2\sqrt{km}\zeta_{air}$, respectively, where ζ_{air} is the structural damping ratio in air.

To measure the cylinder displacement, a non-contact digital optical linear encoder (model: RGH24; Renishaw, UK) was used, which had a resolution of 1 μm and a linear measurement range of ± 200 mm. For a vibrating cylinder, while the streamwise fluid force (F_x) was measured directly using a customised force balance, the transverse lift force (F_y) was determined based on Eq. (1), where the body velocity and acceleration ($\dot{y}$ and $\ddot{y}$) were derived from the cylinder displacement (y). Validations of this method can be found in Zhao et al. (2014b, 2018b). The signals of the body displacement and fluid forces were acquired simultaneously at a sampling frequency of 100 Hz for 300 s (more than 100 vibration cycles). The reduced velocity, given by $U^* = U/(f_{nw}b)$, was investigated over the range of $1.6 \leqslant U^* \leqslant 14$, where U is the free-stream velocity. The free-stream velocity was varied in the range of $43 \lesssim U \lesssim 322$ mm s^{-1}, with the turbulence level less than 1%. The corresponding Reynolds number range was $860 \leqslant Re \leqslant 8050$.

3. Results and discussion

While the focus of the present study aims to examine the FIV response of elliptical cylinders with low elliptical ratios ($0.67 \leqslant \epsilon \leqslant 1.50$), this section presents analytical results of the dynamic responses, including the structural vibration amplitude and frequency responses, and the fluid forcing components, as the elliptical ratio varies.
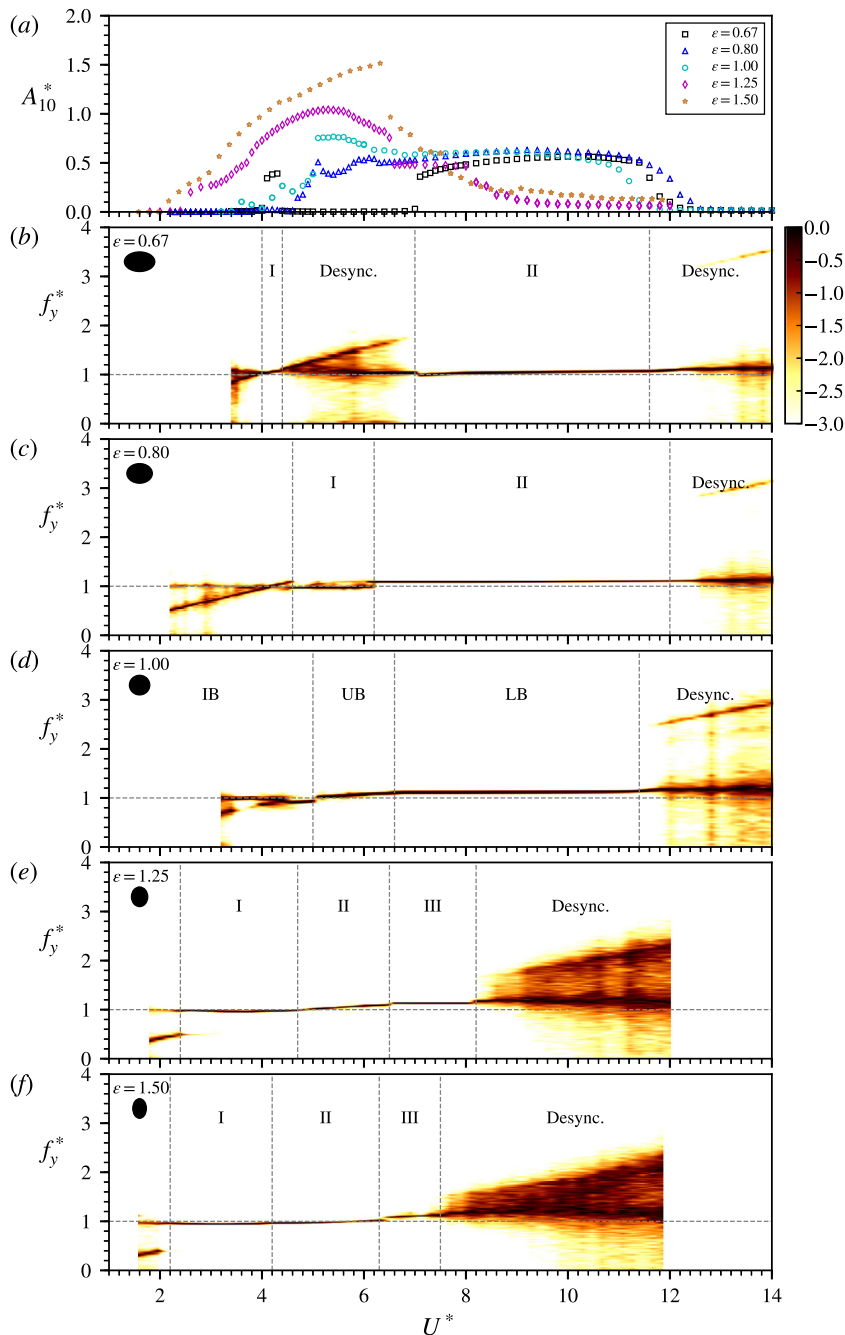
Fig. 2. The normalised amplitude and the logarithmic-scale normalised frequency PSD contours as a function of the reduced velocity for various elliptical ratios. The vertical dashed lines represent boundaries of response regimes in (b–f), while the horizontal dashed line represents f_{nw}. IB: the initial branch, UB: the upper branch and LB: the lower branch.

Fig. 2 shows the normalised vibration amplitude (A_{10}^*) response together with the normalised power spectral density (PSD) contours of the body vibration frequency responses (f_y^*) as a function of the reduced velocity for the five elliptical cylinders tested, while Fig. 3 shows the corresponding PSD contours of the transverse lift force frequency ($f_{C_y}^*$). It should be noted that in this study the normalised amplitude is denoted by A_{10}^*, which represents the mean of the top 10% amplitude peaks normalised by b (see Nemes et al., 2012; Zhao et al., 2014b). The frequency PSD contour plots are constructed by stacking horizontally the PSD (normalised by the local maximum value) of the time series at each tested U^*, noting that f^* denotes the cylinder oscillation frequency normalised by f_{nw}. The coefficients of the streamwise and transverse fluid
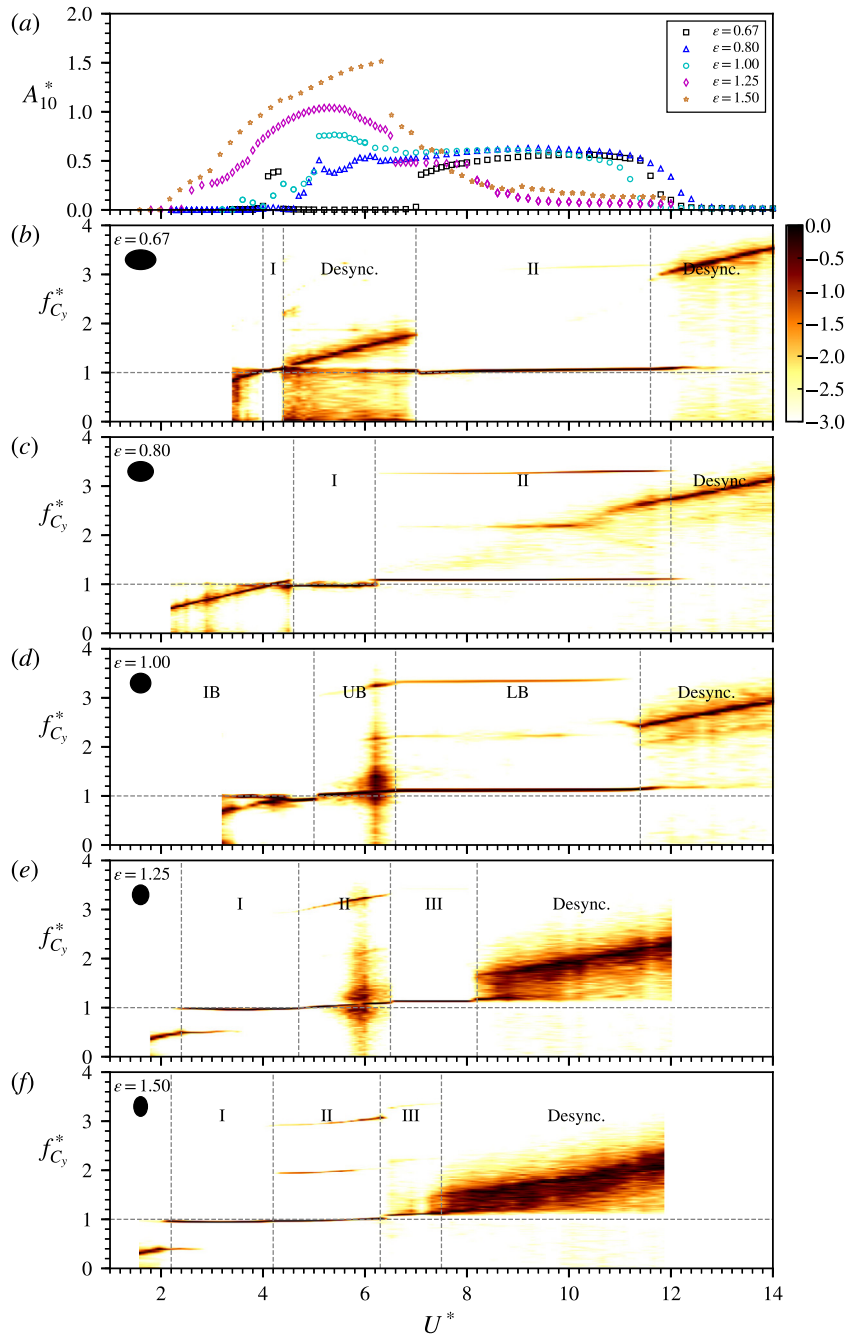
Fig. 3. The normalised amplitude and the logarithmic-scale normalised frequency PSD contours of the transverse lift as a function of the reduced velocity for various elliptical ratios. For more details, see the caption of Fig. 2.

forces used in this study are defined by $C_x = F_x/(\frac{1}{2}\rho U^2 bL)$ and $C_y = F_y/(\frac{1}{2}\rho U^2 bL)$, respectively; the vortex force coefficient is defined by $C_v = F_v/(\frac{1}{2}\rho U^2 bL)$, where the vortex force is decomposed from the transverse lift by $F_v = F_y - F_p$, with $F_p = -m_A\ddot{y}$ the potential force (see Lighthill, 1986; Govardhan and Williamson, 2000; Morse and Williamson, 2009; Zhao et al., 2014a).

As can be seen in Fig. 2(a), the ellipses exhibit distinctly different amplitude responses as the elliptical ratio varies. Firstly, as a reference, the circular cylinder case ($\epsilon = 1$) sees a typical three-branch VIV response. The initial branch (IB) is observed for low reduced velocities $U^* < 5.0$, which is followed by an abrupt jump the upper branch (UB) over $5.0 \leqslant U^* < 6.6$. The lower branch (LB) covers the reduced velocity range $6.6 < U^* < 11.4$. Both the upper and lower branches are associated with lock-in phenomena. For reduced velocities beyond the lower branch, the vortex shedding frequency and the body vibration
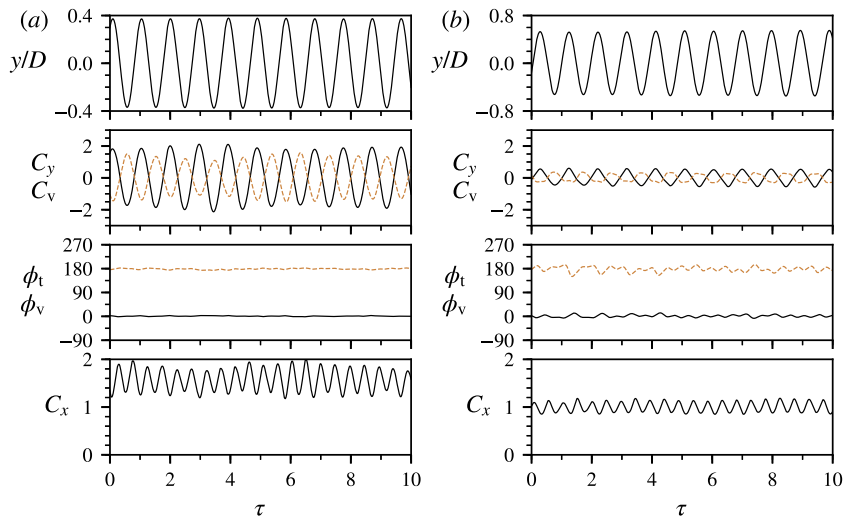
Fig. 4. Sample time traces of the body displacement (y/D), fluid force coefficients (C_y, C_v and C_x) and phases (ϕ_t and ϕ_v) for $\epsilon = 0.67$ at (a) $U^* = 4.2$ and (b) $U^* = 10.0$. Note that the phases are presented in degrees.

frequency become desynchronised. These results are consistent with previous studies with similar low mass and damping ratios (e.g. Zhao et al., 2018b). For the lowest elliptical ratio tested, $\epsilon = 0.67$, the most striking feature is the appearance of two significant vibration regimes. These two regimes are found to be lock-in regimes, as evidenced by the responses of f_y^* and $f_{C_y}^*$ shown in Figs. 2(b) and 3(b), where the body vibration frequency matches the transverse lift frequency (i.e., $f_y^* \cong f_{C_y}^* \simeq 1$). The appearance of the two separated lock-in regimes is significantly different from the numerical results at a low Reynolds number ($Re = 200$) by Leontini et al. (2018), where one lock-in regime occurs over the range of $2.5 \lesssim U^* \lesssim 3.5$. In the present study, the first lock-in regime (regime I) occurs over a very narrow range of $4.0 \lesssim U^* \lesssim 4.4$, when the vortex shedding frequency coincides with f_{nw}. Compared to the circular cylinder case, the onset of lock-in occurs at a much lower reduced velocity, with the body oscillation amplitude ($A_{10}^* \approx 0.38$) much lower than that of the circular cylinder at the onset of lock-in (the beginning of the upper branch). The second lock-in regime (regime II) covers the range of $7.0 \leqslant U^* \leqslant 11.6$, which is similar to the range where the lower branch of the circular cylinder occurs. In this regime, the vibration amplitude is observed to be $A_{10}^* \approx 0.55$, comparable to that seen in the lower branch of the circular cylinder. Moreover, in the two lock-in regimes, the dynamics are highly periodic. To demonstrate this, Fig. 4 shows sample time traces of the body displacement, the fluid force coefficients, and the total and vortex phases at $U^* = 4.2$ (regime I) and $U^* = 10.0$ (regime II). It should be noted that in this study the total phase (ϕ_t) refers to the phase angle between the transverse lift and the body displacement, and the vortex phase (ϕ_v) refers to the phase angle between the vortex force and the body displacement. As shown in this figure, the dynamics are highly periodic in the two U^* cases; however, the total phase ($\phi_t \approx 0°$) and the vortex phase ($\phi_v \approx 180°$) remain similar in both cases, which is different to the circular cylinder case where there are distinct changes in the phases for different vibration response regimes (i.e. ϕ_v: $0° \to 180°$ for the initial branch $\to$ the upper branch, and ϕ_t: $0° \to 180°$ for the upper branch $\to$ the lower branch). The variations of the phases as a function of the reduced velocity are given in Fig. 5. Outside the two lock-in regimes, the fluid–structure interaction appears to be desynchronised, where frequency responses are split into two broadbands, with one following the trend of the Strouhal vortex shedding frequency and the other close to the natural frequency.

As ϵ is increased to 0.80, lock-in occurs over the reduced velocity range of $4.6 \lesssim U^* \lesssim 12.0$, within which two response regimes (I and II) are identified based on the frequency responses and the phases. Regime I covers the range of $4.6 \lesssim U^* < 6.2$, where the body vibration frequency matches f_{nw} (i.e. $f_y^* \simeq 1$). Noticeably, the onset of this regime occurs at a reduced velocity higher than that of the $\epsilon = 0.67$ case, when the body vibration frequency, which tends to follow the Strouhal vortex frequency at low U^* values, passes through the natural frequency to $f_y^* \simeq 1.1$. Compared to the circular cylinder, on the other hand, although the occurrence U^* range of this regime seems to be similar to that of the upper branch, the A_{10}^* response appears to be much lower, with the local peak observed to be $A_{10}^* \simeq 0.56$ at $U^* = 5.1$. With U^* increased to regime II ($6.2 < U^* \leqslant 12.0$), while the vibration frequency becomes consistent at $f_y^* \simeq 1.1$, the vibration amplitude appears to be fairly stable at $A_{10}^* \approx 0.6$. Furthermore, from the dynamic responses shown in Fig. 5, it can be seen that the variations of ϕ_t and ϕ_v in the lock-in regimes appear to be similar to those of the $\epsilon = 0.67$ case, while the variations of the root-mean-square (RMS) coefficients of the transverse lift and vortex forces (C_y^{RMS} and C_v^{RMS}) exhibit trends similar to the circular cylinder case.

For the higher elliptical ratio of $\epsilon = 1.25$, the FIV response exhibits three lock-in regimes (I, II and III) and a desynchronisation region. In general, the amplitude response of this case appears to be similar to the three-branch response of the circular cylinder. Surprisingly, however, the onset of regime I occurs at a very low reduced velocity of $U^* = 2.4$,
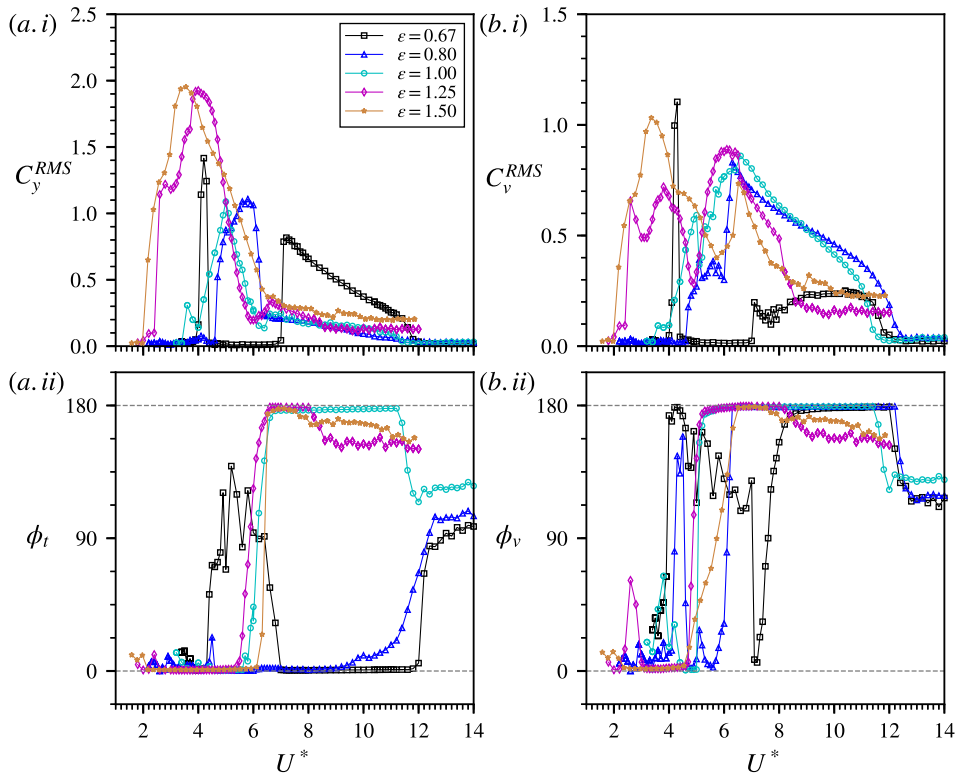
Fig. 5. Variations of the root-mean-square coefficients of the transverse lift and vortex forces (C_y^{RMS} and C_v^{RMS}), together with the total and vortex phases (ϕ_t and ϕ_v), as a function of U^* for the ϵ cases tested. Note that the phases are presented in degrees.

when the vibration frequency becomes locked onto f_{nw}. As a result, the vibration amplitude undergoes a small jump and then increases gradually with U^*. Meanwhile, as shown in Fig. 5, both ϕ_t and ϕ_v remain consistently at $0°$ for U^* up to 4.7. While ϕ_t still remains consistently at $0°$ as U^* is further increased, ϕ_v undergoes a rapid jump to approximately $180°$, which is indicative of the onset of regime II. This transition is very similar to that of the initial branch to the upper branch, in terms of the onset U^* and the jump in ϕ_v. On the other hand, ϕ_t experiences a transition to approximately $180°$ at $U^* = 6.5$, which denotes the upper boundary of this regime. Similarly to the upper branch of the circular cylinder case, regime II sees the largest body oscillations for this ϵ case. The peak amplitude is observed to be $A_{10}^* \simeq 1.05$ at $U^* = 5.6$, an increase of 36% against the circular cylinder case. As the FIV response reaches regime III, the vibration amplitude response drops to a plateau of $A_{10}^* \simeq 0.48$ over $6.5 < U^* \lesssim 8.2$. Moreover, associated with the transition to regime III, ϕ_t undergoes a rapid jump from $0°$ to $180°$, similar to the transition of the upper branch to the lower branch for the circular cylinder case. For higher U^* values, the body oscillations become desynchronised. For the case of $\epsilon = 1.50$, the FIV response regimes are in general similar to the $\epsilon = 1.25$ case, but they tend to occur at slightly lower U^* values. The A_{10}^* peak value is observed to be 1.52 at $U^* = 6.3$, an increase of almost 100% against the circular cylinder case. Correspondingly, substantial increases are also seen in the C_y^{RMS} peaks of these two ϵ cases, while the variations of C_v^{RMS} exhibit similar trends for $\epsilon \geqslant 0.80$ in Fig. 5. Furthermore, compared to the low-*Re* numerical simulations of Leontini et al. (2018), the present case exhibits large-amplitude oscillations over a similar U^* range, but, again, with much larger amplitudes ($\sim 50\%$). This difference is likely due, at least in part, to differences between the two- and three-dimensional flows.

It can be seen from the presented results that the aspect ratio is an important parameter affecting the FIV response of an elliptical cylinder, as it alters the afterbody. Surprisingly, much larger body oscillations are encountered as the afterbody is reduced with increases in the elliptical ratio. Nevertheless, the results suggest that the FIV responses of the elliptical cylinders tested are dominated by VIV rather than transverse galloping, as evidenced by fluid forcing being out of phase with the body movement velocity by approximately $90°$ (i.e. ϕ_t is observed to be close to $0°$ or $180°$) in the regimes where large body oscillations occur.

4. Conclusions

The flow-induced vibration response of elliptical cylinders with a low mass ratio of 6.0 has been examined for various elliptical ratios ranging from 0.67 to 1.50, over a reduced velocity range of $1.6 \leqslant U^* \leqslant 14$ at moderate Reynolds number. The

results show that the FIV response is strongly related to the elliptical ratio. For $\epsilon = 0.67$, there exist two separated lock-in regimes. The first lock-in regime occurred over $4.0 \lesssim U^* \lesssim 4.4$, when the vortex shedding frequency coincided with f_{nw}, while the second regime occurred over $7.0 \leqslant U^* \leqslant 11.6$, where the vibration amplitude was found to be comparable to that seen in the lower branch of the circular cylinder case. For $\epsilon = 0.8$, lock-in occurred over the reduced velocity range $4.6 \lesssim U^* \lesssim 12.0$, within which two response regimes were identified. For this case, the amplitude response is found to be similar to that of the circular cylinder, but without an upper branch. For the cases of $\epsilon = 1.25$ and 1.50, the FIV response exhibits three regimes associated with lock-in phenomenon, which are to some extent similar to the three-branch VIV response of a circular cylinder. However, in these two elliptical cases, the oscillation amplitude grew rapidly once the lock-in occurs at much lower reduced velocities. The A_{10}^* peak values were observed to be 1.05 (an increase of 36% against the circular cylinder case) for $\epsilon = 1.25$ and 1.56 (an increase of almost 100% against the circular cylinder case) for $\epsilon = 1.50$. Significantly, it is found that the peak vibration amplitude tends to increase as the afterbody is reduced with increases in the elliptical ratio above unity. The results indicate that for the present low-aspect-ratio elliptical cylinders, the FIV response is dominated by vortex-induced vibration, rather than transverse galloping.

Further investigation on the wake structure would be of great interest to gain a deeper understanding of the fluid–structure mechanism and physics behind the present findings.

Acknowledgements

References

Bearman, P.W., 1984. Vortex shedding from oscillating bluff bodies. Annu. Rev. Fluid Mech. 16 (1), 195–222.

Bearman, P.W., Gartshore, I.S., Maull, D., Parkinson, G.V., 1987. Experiments on flow-induced vibration of a square-section cylinder. J. Fluids Struct. 1 (1), 19–34.

Blevins, R.D., 1990. Flow-Induced Vibration, second ed. Krieger Publishing Company, Malabar.

Brooks, P.H.N., 1960. Experimental investigation of the aeroelastic instability of bluff two-dimensional cylinders. M.A.Sc. University of British Columbia.

Carberry, J., Sheridan, J., Rockwell, D., 2005. Controlled oscillations of a cylinder: forces and wake modes. J. Fluid Mech. 538, 31–69.

D'Alessio, S.J.D., Kocabiyik, S., 2001. Numerical simulation of the flow induced by a transversely oscillating inclined elliptic cylinder. J. Fluids Struct. 15 (5), 691–715.

Den Hartog, J.P., 1932. Transmission line vibration due to sleet. Trans. Amer. Inst. Electr. Eng. 51 (4), 1074–1076.

Feng, C.C., 1968. The measurement of vortex induced effects in flow past stationary and oscillating circular and D-section cylinders (Master's thesis), The University of British Columbia.

Franzini, G.R., Fujarra, A.L.C., Meneghini, J.R., Korkischko, I., Franciss, R., 2009. Experimental investigation of vortex-induced vibration on rigid, smooth and inclined cylinders. J. Fluids Struct. 25 (4), 742–750.

Gabbai, R.D., Benaroya, H., 2005. An overview of modeling and experiments of vortex-induced vibration of circular cylinders. J. Sound Vib. 282 (3–5), 575–616.

Govardhan, R., Williamson, C.H.K., 2000. Modes of vortex formation and frequency response of a freely vibrating cylinder. J. Fluid Mech. 420, 85–130.

Govardhan, R., Williamson, C.H.K., 2006. Defining the 'modified Griffin plot' in vortex-induced vibration: revealing the effect of Reynolds number using controlled damping. J. Fluid Mech. 561, 147–180.

Johnson, S.A., Thompson, M.C., Hourigan, K., 2004. Predicted low frequency structures in the wake of elliptical cylinders. Eur. J. Mech. B Fluids 23 (1), 229–239.

Khalak, A., Williamson, C.H.K., 1996. Dynamics of a hydroelastic cylinder with very low mass and damping. J. Fluids Struct. 10 (5), 455–472.

Kim, M.S., Park, Y.B., 2006. Unsteady lift and drag forces acting on the elliptic cylinder. J. Mech. Sci. Technol. 20 (1), 167–175.

Kim, M.-S., Sengupta, A., 2005. Unsteady viscous flow over elliptic cylinders at various thickness with different reynolds numbers. J. Mech. Sci. Technol. 19 (3), 877–886.

Leontini, J.S., Griffith, M., Jacono, D.L., Sheridan, J., 2018. The flow-induced vibration of an elliptical cross-section at varying angles of attack. J. Fluids Struct. 78, 356–373.

Leontini, J.S., Jacono, D.L., Thompson, M.C., 2015. Stability analysis of the elliptic cylinder wake. J. Fluid Mech. 763, 302–321.

Lighthill, J., 1986. Fundamentals concerning wave loading on offshore structures. J. Fluid Mech. 173, 667–681.

Lindsey, W.F., 1938. Drag of cylinders of simple shapes. NACA Tech. Repor 619, 169–176.

Morse, T.L., Williamson, C.H.K., 2009. Prediction of vortex-induced vibration response by employing controlled motion. J. Fluid Mech. 634, 5–39.

Nair, M.T., Sengupta, T.K., 1997. Unsteady flow past elliptic cylinders. J. Fluids Struct. 11 (6), 555–595.

Naudascher, E., Rockwell, D., 2005. Flow-Induced Vibrations: An Engineering Guide. Dover Publications.

Nemes, A., Zhao, J., Lo Jacono, D., Sheridan, J., 2012. The interaction between flow-induced vibration mechanisms of a square cylinder with varying angles of attack. J. Fluid Mech. 710, 102–130.

Okajima, A., Takata, H., Asanuma, T., 1975. Viscous flow around a transversally oscillating elliptic cylinder. Report, Inst. Space Aeronaut. Sci., Univ. Tokyo 40 (13), 339.

Ota, T., Nishiyama, H., Taoka, Y., 1987. Flow around an elliptic cylinder in the critical Reynolds number regime. J. Fluids Eng. 109 (2), 149–155.

Païdoussis, M., Price, S., De Langre, E., 2010. Fluid-Structure Interactions: Cross-Flow-Induced Instabilities. Cambridge University Press.

Rao, A., Leontini, J.S., Thompson, M.C., Hourigan, K., 2017. Three-dimensionality of elliptical cylinder wakes at low angles of incidence. J. Fluid Mech. 825, 245–283.

Sareen, A., Zhao, J., Jacono, D.L., Sheridan, J., Hourigan, K., Thompson, M.C., 2018a. Vortex-induced vibration of a rotating sphere. J. Fluid Mech. 837, 258–292.

Sareen, A., Zhao, J., Sheridan, J., Hourigan, K., Thompson, M.C., 2018b. The effect of imposed rotary oscillation on the flow-induced vibration of a sphere. J. Fluid Mech. 855, 703–735.

Sareen, A., Zhao, J., Sheridan, J., Hourigan, K., Thompson, M.C., 2018c. Vortex-induced vibrations of a sphere close to a free surface. J. Fluid Mech. 846, 1023–1058.

Sarpkaya, T., 2004. A critical review of the intrinsic nature of vortex-induced vibrations. J. Fluids Struct. 19 (4), 389–447.

Sheard, G., 2007. Cylinders with elliptical cross-section: wake stability with incidence angle variation. In: Proceedings of the IUTAM Symposium on Unsteady Separated Flows and their Control. pp. 5–18.

Soti, A.K., Zhao, J., Thompson, M.C., Sheridan, J., Bhardwaj, R., 2018. Damping effects on vortex-induced vibration of a circular cylinder and implications for power extraction. J. Fluids Struct. 81, 289–308.

Thompson, M.C., Radi, A., Rao, A., Sheridan, J., Hourigan, K., 2014. Low-Reynolds-number wakes of elliptical cylinders: from the circular cylinder to the normal flat plate. J. Fluid Mech. 751, 570–600.

Wang, Z., Du, L., Zhao, J., Sun, X., 2017. Structural response and energy extraction of a fully passive flapping foil. J. Fluids Struct. 72, 96–113.

Williamson, C.H.K., Govardhan, R., 2004. Vortex-induced vibration. Annu. Rev. Fluid Mech. 36, 413–455.

Wong, K.W.L., Zhao, J., Lo Jacono, D., Thompson, M.C., Sheridan, J., 2017. Experimental investigation of flow-induced vibration of a rotating circular cylinder. J. Fluid Mech. 829, 486–511.

Wong, K.W.L., Zhao, J., Lo Jacono, D., Thompson, M.C., Sheridan, J., 2018. Experimental investigation of flow-induced vibration of a sinusoidally rotating circular cylinder. J. Fluid Mech. 848, 430–466.

Yogeswaran, V., Sen, S., Mittal, S., et al., 2014. Free vibrations of an elliptic cylinder at low reynolds numbers. J. Fluids Struct. 51, 55–67.

Zhao, J., Hourigan, K., Thompson, M.C., 2018a. Flow-induced vibration of D-section cylinders: an afterbody is not essential for vortex induced vibration. J. Fluid Mech. 851, 317–343.

Zhao, J., Leontini, J.S., Lo Jacono, D., Sheridan, J., 2014a. Chaotic vortex induced vibrations. Phys. Fluids 26 (12), 121702.

Zhao, J., Leontini, J.S., Lo Jacono, D., Sheridan, J., 2014b. Fluid–structure interaction of a square cylinder at different angles of attack. J. Fluid Mech. 747, 688–721.

Zhao, J., Lo Jacono, D., Sheridan, J., Hourigan, K., Thompson, M.C., 2018b. Experimental investigation of in-line flow-induced vibration of a rotating cylinder. J. Fluid Mech. 847, 664–699.

Zhao, J., Nemes, A., Lo Jacono, D., Sheridan, J., 2018c. Branch/mode competition in the flow-induced vibration of a square cylinder. Philos. Trans. R. Soc. Lond. Ser. A 376, 20170243.